Linear and nonlinear hydrodynamic models for dynamics of a submerged point absorber wave energy converter

Benjamin Schubert, William S P Robertson, Benjamin Cazzolato, Mergen Ghayesh

School of Mechanical Engineering, University of Adelaide, Australia

Abstract

This study compares the response of a submerged CETO-shaped point absorber wave energy converter using linear, partially-nonlinear, pseudo-nonlinear, and fully-nonlinear methods to model hydrodynamic effects. Linear potential flow models calculate hydrodynamic parameters to represent the fluid-structure interaction; typical dynamic models apply these parameters without pose-dependence. The partially-nonlinear method evaluates excitation forces at different poses to introduce a pose-dependent excitation force; in addition to the excitation force, the pseudo-nonlinear method calculates hydrodynamic coefficients using linear potential flow methods and includes pose-dependence through interpolating pre-calculated parameters to represent the radiation force. The fully-nonlinear CFD model is a numerical wave tank validated against published data. The applicability of linear-based methods has been explored by comparing the motion, force, and power of the system under various operating conditions against the fully-nonlinear results. It was expected that for low amplitude waves results tend towards the linear results; however, for both low amplitude waves and increased submergence depth, linear methods provided poor representations of the nonlinear CFD results. Geometric nonlinearities were insufficient to capture all the nonlinear behaviour. A frequency-dependent nonlinearity was identified in the water above the buoy resonating. For such submerged point absorbers, linear methods do not adequate represent the influential nonlinear effects.

Keywords: wave energy converter; submerged point absorber; fully and partially nonlinear hydrodynamics; numerical wave tank

1. Introduction

The concept of harvesting ocean wave energy has been in development for over two centuries (Cruz, 2008). As demand for power moves towards renewable sources of energy, a world-wide interest has been building since the 1970s. A variety of different devices and operation principles have been proposed in literature and in practice (Drew et al., 2009). These devices are primarily in the research and prototype stage (Hardy et al., 2016), and require further development to achieve economic viability for large scale energy production (Chozas, 2015). Specifically, high fidelity modelling is an essential part of the design stage. Faster modelling techniques would benefit both research and commercial efforts.

A point absorber (PA) is a common wave energy converter (WEC), is small relative to an incident wave (Cruz, 2008), and can be either floating or submerged, as shown schematically in Figure 1. For designing such devices, efficient and accurate computational models of the system dynamics are essential. These modelling methods can be used to estimate device performance, implement and test control systems, and are more cost effective than constructing a prototype. The device modelled and analysed in this study is based on a CETO-like device previously studied (Rafiee and Fiévez, 2015) and is a cylindrically shaped device that is nominally submerged, as shown in Figure 2. To model WEC systems, typical methods include using linear boundary element method (BEM) solvers such as ANSYS Aqwa (ANSYS, Inc., Canonsburg PA, USA), WAMIT (WAMIT, Inc., Chestnut Hill MA, USA), and NEMOH (L'École Centrale De Nantes, Nantes, France), to find various hydrodynamic parameters. Simulations of the model dynamics can use these parameters to quantify various hydrodynamic forces acting on the buoy. An alternative approach, which is fully nonlinear, is the computationally intensive numerical wave tank (NWT) CFD approach. NWT are becoming increasingly common within research communities and industry (Windt et al., 2018).

The BEM (used for wave energy applications) and CFD approaches are considered linear and nonlinear in principle, respectively. The benefits of BEM techniques include fast solutions suited to studies requiring many iterations such as optimisation. As the BEM is linear, they do not account of nonlinearities seen in the fluid-structure interaction such as overtopping, slamming, flow separation, or viscosity. Additionally, BEM techniques provide the hydrodynamic parameters about a nominal pose and ignore geometric nonlinearities associated with a change of position and orientation. It has been shown that results from linear BEM solvers rapidly lose accuracy as the buoy deviates from the nominal position and nonlinearities become more influential (Davidson et al., 2015).

Fully nonlinear CFD approachs use numerical solvers based on the Navier Stokes equation (Penalba et al., 2017a). These

Email address: benjamin.schubert@adelaide.edu.au (Benjamin Schubert)

models should be validated experimentally to ensure high fidelity reliable results (Windt et al., 2018). Typical CFD methods are computationally intensive and are often not validated against experimental results. While computational resources are becoming more readily available, alternative techniques to capture nonlinear effects using faster approaches would provide valuable improvements to current modelling techniques.

The most relevant nonlinearity for small heaving PA WEC systems is considered to be within the excitation force (Penalba et al., 2017a) as it may capture parametrically excited motions not found in simple linear representations. Furthermore, for small heaving PA WEC system, diffraction and radiation effects are typically small compared to the Froude-Krylov force, one component of the excitation force (Giorgi and Ringwood, 2017a). Accordingly, previous attempts to capture nonlinear effects have focussed on the hydrodynamic excitation force. Such attempts include: extending the linear potential flow model to a fully nonlinear potential flow model (Guerber et al., 2012); recalculating the hydrodynamic forces at each time step with the linear solver (Penalba et al., 2017c; Merigaud et al., 2012); partially extending the hydrodynamic force to a second order approximation (Merigaud et al., 2012); using a gain scheduling method to include the impact of orientation on hydrodynamic parameters (McCabe et al., 2006). Extending the hydrodynamic forces found from BEM solvers by considering the instantaneous pose dependence is often termed partially nonlinear within literature (Penalba et al., 2017a). These methods demonstrate some improvement compared to the linear model but are often only suited to particular circumstances. Most of these methods (Penalba et al., 2017c; Merigaud et al., 2012; McCabe et al., 2006) are applied to *floating* buoys for which the hydrodynamic parameters are heavily dependent on wetted area. Submerged buoys, however, have a significantly different depth dependence, independent of wetted area. The fully nonlinear potential flow model (Guerber et al., 2012) pertains to a submerged cylindrical PA which has small dimensions and is subject to low amplitude waves. Such conditions predispose linear models to give acceptable results. While such nonlinear potential flow models appear promising, it is commonly accepted that such techniques for calculating hydrodynamic properties require further research (Penalba et al., 2017a). Another alternative is the weak-scatterer approach where the free surface conditions on the instantaneous wave elevation is linearised, and the fluid-structure interactions are calculated for exact positions. This model has been applied to a submerged buoy, and has been shown to agree with linear models for linear conditions and demonstrate significant deviations from linear theory for nonlinear conditions (Letournel et al., 2018). The importance of including nonlinear effects for control systems for wave energy systems has been demonstrated through the introduction of two nonlinear measures for wave-to-wire models (Penalba and Ringwood, 2019). One measurement was related to the hydrodynamic interaction and the other refers to the nonlinear effects in the power take-off (PTO).

Recently, some effort have been made to assess the pressure field accuracy for representing the Froude-Krylov force (Giorgi and Ringwood, 2017b). It was found that for a heaving PA, Wheeler's stretching method of Airy's linear wave theory was suitable to capture nonlinearity assuming small radiation and diffraction forces. This method was applied to a six degree of freedom (DOF) model (Giorgi and Ringwood, 2019) and showed how such nonlinearities impact power generation. However, no CFD or fully nonlinear model was presented for validation purposes, and the device modelled was floating and far smaller than the CETO shaped device presented in this study. A reconfigurable oscillating surge wave energy converter has also been modelled using multiple linear hydrodynamic gains with some success (Papillon et al., 2019). Additionally, for this type of oscillating surge device, an enhanced nonlinear time domain numerical model in which pitch angle dependence was introduced in the excitation torque and a nonlinear representation of the radiation torque, was shown to improve the estimated torques when compared to experimental results (Crooks, 2017).

Models of WEC systems are often restricted to one or two degrees of freedom, depending on the mode of operation of the buoy. However, for submerged multi-DOF PA WECs, the change of hydrodynamic parameters which couple DOF for varying poses (particularly orientations) may be significant in capturing coupling between DOF and other oscillatory modes. This change of hydrodynamic parameters due to pose is fundamental to the operation of such systems. Overall, it is generally expected that linear models overestimate WEC performance (Rafiee and Fiévez, 2015), as many hydrodynamic nonlinearities are neglected. For the context of submerged buoys, comparisons between linear and nonlinear modelling techniques remains an area of ongoing research.

Previous work on a pseudo-nonlinear modelling technique incorporates pose dependence in the hydrodynamic parameters (Schubert et al., 2018). Previously, two buoys were analysed: a cylindrical buoy, for which the hydrodynamic parameters are dependent on position and orientation, and a spherical buoy, for which the hydrodynamic parameters depend only on position due to symmetry. Linear, pseudo-nonlinear, and fully nonlinear hydrodynamic modelling techniques were compared and it was shown that the pseudo-nonlinear method followed the trend of the nonlinear results, but significantly overestimated the performance of the devices. Pseudo-nonlinear results for the spherical buoy were a better approximation of the CFD results than for the cylindrical buoy. The buoys differed in size, were close to the surface, and were subject to regular waves of 1m height. These findings indicate a significant dependence on operating conditions such as submergence depth and wave amplitude.

This paper extends previous work to explore the impact of the submergence depth and wave height on the validity of the including pose dependent hydrodynamic nonlinearity when looking at the dynamic performance of a submerged PA WEC. A comparison between a linear, partially nonlinear, pseudo-nonlinear, and fully nonlinear models will be presented for varying wave heights and submergence depths. The 3DOF models are subject to regular waves and include surge, heave, and pitch hydrodynamic dependence. The linear model uses hydrodynamic parameters about a nominal position, which are found using the BEM solver NEMOH. For the context of wave energy devices, a comparison between NEMOH and WAMIT was

conducted (Penalba et al., 2017b). This comparison concluded that for submerged point absorbers, such as the WEC considered in the present study, the difference between open source solver NEMOH and the commercially available solver WAMIT is minimal.

The linear model ignores any spatial nonlinearities in the hydrodynamic forces, but includes the geometric nonlinearities associated with the direction of the PTO force inherent in 3DOF modelling. The partially nonlinear model uses linear hydrodynamic forces, and introduces pose dependence through gain-scheduling the excitation force. The pseudo-nonlinear method uses the same BEM solver to provide the hydrodynamic parameters at a series of locations over the motion amplitude. Linearly interpolating these values at a given position for each time step provides pose-dependent hydrodynamic parameters to represent radiation forces as well as pose-dependent excitation forces. A NWT in OpenFOAM has been constructed and validated against experimental data available in literature (Rafiee and Fiévez, 2015). This validated fully nonlinear model is used to infer the accuracy of the linear and pseudo-nonlinear models. One case was analysed in depth and demonstrated significant nonlinear behaviour not represented in any of the three linear based models. A summary of the differences between the modelling approaches is given in Table 1.

The mathematical formulation of the WEC model is provided in Section 2 in the form of equations of motion and a discussion of each relevant force for each modelling technique. Validation of the fully nonlinear CFD model is given in Section 3. The simulation process and parameters of each proposed test scenario is provided in Section 4 with results display in Section 5. The interpretation and implications of these findings are presented in Section 6, with a summary of the process and findings in Section 7.

2. Mathematical Model of WEC

In this study, a cylindrical buoy is modelled in three DOF, with pose represented as

$$\mathbf{x} = \begin{pmatrix} \text{Surge} \\ \text{Heave} \\ \text{Pitch} \end{pmatrix} = \begin{pmatrix} x \\ z \\ \theta \end{pmatrix}. \tag{1}$$

In the time domain, the motion of this system can be described using the modified Cummins equation (Rafiee and Fiévez, 2015), expressed as

$$\mathbf{M}\ddot{\mathbf{x}} = \mathbf{F}_\mathrm{e} + \mathbf{F}_\mathrm{rad} + \mathbf{F}_\mathrm{h} + \mathbf{F}_\mathrm{PTO} + \mathbf{F}_\mathrm{d} \tag{2}$$

where $\mathbf{M}$ is a matrix which contains the inertial terms for each DOF, and $\mathbf{F}_\mathrm{e}$, $\mathbf{F}_\mathrm{rad}$, $\mathbf{F}_\mathrm{h}$, $\mathbf{F}_\mathrm{PTO}$, and $\mathbf{F}_\mathrm{d}$ represent the excitation, radiation, hydrostatic, PTO, and drag force respectively. The methods used to calculate some of these terms vary between the linear, pseudo-nonlinear, and fully nonlinear approaches. Specific descriptions of each term and calculation method is discussed throughout the remainder of this section.

2.1. Excitation force

The excitation force, $\mathbf{F}_\mathrm{e}$, is the superposition of the diffraction and Froude-Krylov forces (Merigaud et al., 2012). Within the linear model, $\mathbf{F}_\mathrm{e}$ is described as

$$\mathbf{F}_\mathrm{e} = \mathbf{F}_\mathrm{e,amp} \circ \cos(\boldsymbol{\sigma} + \sigma_\mathrm{s} - \omega t) \,, \tag{3}$$

where $\mathbf{F}_\mathrm{e,amp}$ and $\boldsymbol{\sigma}$ are the amplitude and phase vectors of the excitation force in 3DOF respectively, t denotes time, and ω is the wave frequency. The Hadamard product operator, $\circ$, is used to indicate element-wise multiplication. The linear model proposes that $\mathbf{F}_\mathrm{e,amp}$ and $\boldsymbol{\sigma}$ are functions only of ω, whereas the pseudo-nonlinear model includes pose dependence, causing the $\mathbf{F}_\mathrm{e,amp}$ and $\boldsymbol{\sigma}$ hydrodynamic parameters to be dependent on $\mathbf{x}$. The heave and pitch directly impact these parameters, while surge changes the location of the buoy relative to the incident wave. Therefore, the impact of the surge position on the phase of the excitation force, σ_s, is quantified by

$$\sigma_\mathrm{s} = kx \,, \tag{4}$$

where k is the wavenumber, which is the solution to (Chao Jiang et al., 2014)

$$\omega^2 = gk \tanh(kh) \,, \tag{5}$$

where h is the water depth, and g is the acceleration due to gravity. The partially nonlinear and pseudo-nonlinear excitation force may be expressed as

$$\mathbf{F}_\mathrm{e}(z, \theta, \omega) = \mathbf{F}_\mathrm{e,amp}(z, \theta, \omega) \circ \cos(\boldsymbol{\sigma}(z, \theta, \omega) + \sigma_\mathrm{s} - \omega t) \,. \tag{6}$$

The partially nonlinear and pseudo-nonlinear representation of the excitation force was accomplished using a discrete gain scheduling method. For each DOF, the operating range was discretised into 13 steps, which necessitates prior knowledge of the approximate bounds of motion. The bounds of the linear model may be considered an appropriate first guess. During simulation, the instantaneous heave and pitch were used to interpolate between the excitation force amplitude and phase for each DOF. A similar interpolation technique has been applied previously for 1DOF floating body (McCabe et al., 2006), and is fundamentally a computationally cheap alternative to recalculating the excitation force at each time step applied in other studies (Penalba et al., 2017c).

2.2. Radiation force

As a buoy oscillates in the fluid, waves are radiated outward. The effective force on the buoy due to this effect is known as the radiation force, $\mathbf{F}_\mathrm{r}$, and can be calculated in the time using the Cummins equation (Cummins, 1962),

$$\mathbf{F}_\mathrm{r} = -\mathbf{A}_\infty \ddot{\mathbf{x}} - \int_0^t \mathbf{K}(t - t')\dot{\mathbf{x}}(t')dt' \,, \tag{7}$$

where $\mathbf{A}_\infty$ and $\mathbf{K}$ represent the infinite frequency added mass and memory function, respectively. This memory function and integral quantifies the impact of the past state of the fluid on the

current state. The radiation force in the frequency domain may be represented as

$$\hat{\mathbf{F}}_{\mathrm{r}} = -[\mathbf{B}(\omega) + i\omega\mathbf{A}(\omega)]\hat{\dot{\mathbf{x}}}(i\omega)\,, \tag{8}$$

where $\mathbf{B}(\omega)$ is the radiation damping and $\mathbf{A}(\omega)$ is the added mass, both of which are frequency-dependent. A well established method in WEC modelling uses the hydrodynamic parameters $\mathbf{B}(\omega)$ and $\mathbf{A}(\omega)$ to construct a transfer function to identify the relationship between the velocity and the integral in Equation (7) (Perez and Fossen, 2009). Fifth order transfer functions were used in the construction of this system representation as these were found to approximately fit the numerical data provided from NEMOH. The linear and partially nonlinear models assume that the hydrodynamic parameters $\mathbf{B}(\omega)$ and $\mathbf{A}(\omega)$ are only frequency dependent, whereas the pseudo-nonlinear method introduces position dependence by representing the system as a series of state space models which depend on the coordinates z and θ. This method was implemented in a Simulink simulation through the use of a linear parameter varying (LPV) block to represent the radiation force using position and velocity as inputs. This LPV technique is a method to represent a model with dynamics that vary as a function of time-varying parameters. In this case, the time-varying parameters are heave and pitch, and the previously calculated grid of state-space representations are used to interpolate for the radiation force. Further information on LPV systems may be found within Matlab documentation (MathWorks, 2019).

2.3. Hydrostatic and PTO forces

The hydrostatic force is common in all models and acts only the z direction, represented by

$$F_{\mathrm{h,z}} = \rho g V - mg\,, \tag{9}$$

where ρ is the density of water, V is the volume of the buoy, and m is the mass of the buoy. This force is constant for submerged buoys and is compensated by a constant force from the PTO. The variable PTO force is modelled as a spring-damper arrangement such that,

$$\mathbf{F}_{\mathrm{PTO}} = \mathbf{T}(-b_{\mathrm{PTO}}\Delta\dot{l} - k_{\mathrm{PTO}}\Delta l - |\mathbf{F}_{\mathrm{h,z}}|)\,, \tag{10}$$

with b_{PTO} and k_{PTO} being the damping coefficients and spring constants respectively, and Δl being the tether extension of the WEC. By extending the model to 3DOF, this introduces nonlinear relationship between terms through the PTO force (Orszaghova et al., 2019), as seen in Equation (10) in the form of a transformation $\mathbf{T}$. The transformation of coordinates $(x, z, \alpha + \phi) \rightarrow (\Delta l, \alpha, \phi)$, shown in Figure 1, can be described by the set of following equations:

$$\Delta l = \sqrt{(x - a\sin(\alpha+\phi))^2 + (z + l + a - a\cos(\alpha+\phi))^2} - l\,, \tag{11}$$

$$\alpha = \arctan\left(\frac{x - a\sin(\alpha+\phi)}{z + l + a - a\cos(\alpha+\phi)}\right), \tag{12}$$

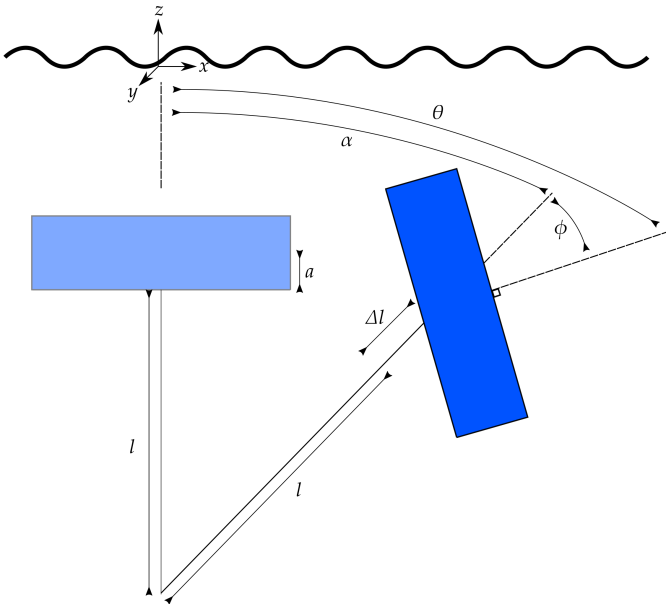

Figure 1: A cylindrical WEC showing two different coordinate systems (surge, heave, pitch) = $(x, z, \theta) \rightarrow (\Delta l, \alpha, \phi)$.

$$\phi = (\phi + \alpha) - \alpha\,, \tag{13}$$

where a and l are the distance between buoy centre and tether attachment point, and the tether length, respectively. It should be noted that $(\phi + \alpha)$ is another representation of pitch, θ, decomposed into two parts, ϕ, the angle of the buoy relative to the tether, and α, the angle of the tether. The rate of change of tether extension, $\Delta\dot{l}$, can be derived by taking the first time derivative of Equation (11), and is given by

$$\Delta\dot{l} = \frac{(x - a\sin(\alpha+\phi))(\dot{x} - a\cos(\alpha+\phi)(\dot{\alpha}+\dot{\phi}))}{\sqrt{(x - a\sin(\alpha+\phi))^2 + (z + l + a - a\cos(\alpha+\phi))^2}} + \frac{(z + l + a - a\cos(\alpha+\phi))(\dot{z} + a\sin(\alpha+\phi)(\dot{\alpha}+\dot{\phi}))}{\sqrt{(x - a\sin(\alpha+\phi))^2 + (z + l + a - a\cos(\alpha+\phi))^2}}\,. \tag{14}$$

The forces and moment from the PTO may then be calculated and applied to the buoy in the initial coordinate system of surge, heave, and pitch, by using simple trigonometric relationships. In the above equations, it is assumed that the tether is fixed at the bottom of an axisymmetric buoy.

The damping and stiffness parameters may be optimised for a given frequency using linear hydrodynamics for a single DOF (Falnes, 2002). By assuming tether extension is primarily associated with vertical motion, optimal conditions are:

$$b_{\mathrm{PTO,\,opt}}(\omega) = B_z(\omega)\,, \qquad k_{\mathrm{PTO,\,opt}}(\omega) = \omega^2(m + A_z(\omega))\,. \tag{15}$$

These equations are valid only for linear hydrodynamics and when the PA is restricted to oscillate in heave, but for the purposes of this study are referred to as optimal conditions. Optimal conditions result in relatively large amplitudes of buoy oscillation, which, for small submergence depths, may result with the buoy breaching the water surface. To prevent breaching,

the optimal stiffness was used, and a sufficiently large damping coefficient common to all scenarios was selected to reduce oscillation amplitude. The values used for stiffness and damping are common to the linear, partially nonlinear, pseudo-nonlinear, and fully nonlinear simulations for the sake of comparison and consistency. The instantaneous power generated, P, may be approximated in all simulations as,

$$P = b_{\mathrm{PTO}} \Delta \dot{l}^2 \ . \tag{16}$$

2.4. Drag force

In fully nonlinear simulations, the drag force, $\mathbf{F}_{\mathrm{D}}$, may be calculated directly at each time step. However, in the linear, partially nonlinear, and pseudo-nonlinear methods, the drag force is approximated using a constant drag coefficient, $\mathbf{C}_{\mathrm{D}}$. The drag force in this case is approximated by

$$\mathbf{F}_{\mathrm{D}} = -\frac{1}{2}\mathbf{C}_{\mathrm{D}}\rho\mathbf{A}_{\mathrm{D}}\dot{\mathbf{x}}_{\mathrm{r}}|\dot{\mathbf{x}}_{\mathrm{r}}| \ , \tag{17}$$

where $\dot{\mathbf{x}}_{\mathrm{r}}$ and $\mathbf{A}_{\mathrm{D}}$ are the velocity of the buoy relative to the surrounding fluid and the characteristic area, respectively. For pitch, the characteristic area is taken to be D^5, where D represents the outer diameter of the buoy, and the velocity is taken to be $\dot{\theta}$ (Sergiienko et al., 2018).

2.5. BEM hydrodynamics calculation

The BEM typically uses potential theory to calculate the excitation and radiation forces at a given frequency for a described buoy (Penalba et al., 2017c). Using Bernoulli's equation, the total pressure can be linearised and expressed as the superposition of four pressure components,

$$p = p_{\mathrm{s}} + p_{\mathrm{d}} + p_{\mathrm{Di}} + p_{\mathrm{r}} \ , \tag{18}$$

where p_{s} and p_{d} represent the static and dynamic pressures respectively, and, p_{Di} and p_{r} represent the pressures associated with the diffraction and radiation forces. The excitation force is the superposition of Froude-Krylov (FK), $\mathbf{F}_{\mathrm{FK}}$, and diffraction forces, $\mathbf{F}_{\mathrm{Di}}$, which are calculated by integrating the respective pressures over the surface of the buoy,

$$\mathbf{F}_{\mathrm{FK}} = -\iint_S p_{\mathrm{d}}\hat{\mathbf{n}}\, dS \ , \qquad \mathbf{F}_{\mathrm{Di}} = -\iint_S p_{\mathrm{Di}}\hat{\mathbf{n}}\, dS \ , \tag{19}$$

where S and $\hat{\mathbf{n}}$ represent the surface and the normal to the surface, respectively. The pressures are derived from analytical formulas for the flow potential. Similarly the radiation force, $\mathbf{F}_{\mathrm{r}}$, can be calculated as

$$\mathbf{F}_{\mathrm{r}} = -\iint_S p_{\mathrm{r}}\hat{\mathbf{n}}\, dS \tag{20}$$

and is subdivided to inertial and damping terms for the $\mathbf{A}$ and $\mathbf{B}$ values from Equation (8). This method has the advantage of being faster than fully nonlinear methods but is linearised and ignores all second order diffraction and radiation terms (Penalba et al., 2017c). For the purpose of this study, the BEM solver NEMOH was used for the linear, partially nonlinear, and pseudo-nonlinear models.

2.6. Model differences summary

The differences between the nonlinearities represented in the four proposed models is summarised in Table 1.

Table 1: Model hydrodynamic nonlinearity summary

Model	**Nonlinear Excitation**	**Nonlinear Radiation**	**Fully Nonlinear**
Linear			
Partially nonlinear	✓		
Pseudo-nonlinear	✓	✓	
CFD	✓	✓	✓

2.7. Fully nonlinear calculation

The fully nonlinear CFD calculations are governed by the Navier-Stokes equations which are a series of fundamental equation capturing the mass continuity, momentum conservation, and energy conservation of the fluid, given by Equations (21), (22), and (23), respectively (Penalba et al., 2017a):

$$\frac{\partial \rho}{\partial t} + \nabla(\rho\mathbf{u}) = 0 \ , \tag{21}$$

$$\frac{\partial u}{\partial t} + (\mathbf{u}\nabla)\mathbf{u} = -\frac{1}{\rho}\nabla\mathbf{p} + \mathbf{F}_{\mathrm{ext}} + \frac{\mu}{\rho}\nabla^2\mathbf{u} \ , \tag{22}$$

$$\rho\left(\frac{\partial \epsilon}{\partial t} + \mathbf{u}\nabla\epsilon\right) - \nabla(K_H\nabla T) + \rho\nabla\mathbf{u} = 0 \ , \tag{23}$$

where $\mathbf{u}$ and μ are the fluid velocity and viscosity, respectively. The pressure field and external force is represented by $\mathbf{p}$ and $\mathbf{F}_{\mathrm{ext}}$. Additionally, ϵ, K_H, and T represent the internal energy, heat conduction coefficient, and temperature.

These equations have the advantage of fully describing the nonlinear behaviour of the fluid. The ensuing fluid-buoy interaction subject to the given fluid conditions may then be solved. As there is no analytical solution, due to complexity, the equations must be solved numerically. Such processes have large computational cost but have been used to simulate WEC systems for decades (Windt et al., 2018). For a CFD model to provide meaningful results, it should be validated. The most trusted method of validation is a comparison against experimental data (Windt et al., 2018).

3. Model Validation

A high fidelity fully nonlinear model was constructed and validated to provide confident comparison between linear, partially nonlinear, pseudo-nonlinear and fully nonlinear simulation scenarios. For the purposes of validation, the geometries of an existing buoy with experimental results (Rafiee and Fiévez, 2015) were used within all simulations. A schematic of the buoy is given in Figure 2, and the corresponding values are provided in Table 2.

The numerical wave tank used in this investigation was constructed in OpenFOAM with dimensions (x, y, z) of $(330, 200, 50)$

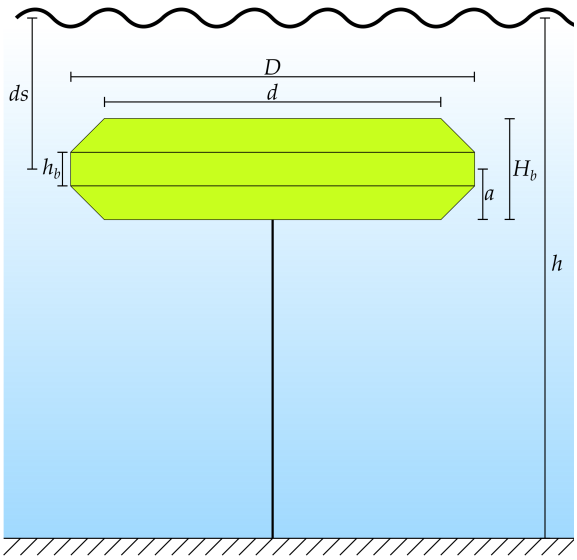

Figure 2: A schematic of the modelled submerged symmetrical CETO-like buoy.

Table 2: CETO-like buoy geometry

Parameter	**Value**	**Units**
Volume, V	1.7475×10^3	m^3
Buoy density, ρ_{buoy}	0.7ρ	$kg\,m^{-3}$
Inner diameter, d	17	m
Outer diameter, D	20	m
Inner height, h_b	3	m
Outer height, H_b	6	m
Attachment arm, a	3	m

metres. The large y dimension reduces boundary effects along the walls. The solver application used was *olaDyMFlow*, which has the advantage of active wave absorption, reducing the necessary relaxation and absorption zones. Though the experimental validation study (Rafiee and Fiévez, 2015) did not provide PTO stiffness and damping parameters, time series data was provided, which enabled estimation of the PTO properties through multivariable regression.

The NWT was first subject to waves without the buoy present and the resolution was increased until convergence in wave height occurred. The buoy was then included but held fixed and the force around the static buoy was checked for convergence and compared to BEM methods. The buoy was then permitted to move in the aforementioned DOF. The whole model was then compared to existing experimental data (Rafiee and Fiévez, 2015). The wave theory used was based on established criteria of wave properties and physical set up (Le Méhauté, 2013). The NWT and WEC specific parameters used in all these simulations are given in Table 3.

Table 3: Validation simulation parameters

Parameter	**Value**	**Units**
Acceleration of gravity, g	9.81	$m\,s^{-2}$
Water density, ρ	1025	$kg\,m^{-3}$
Kinematic viscosity of water, ν	1.004×10^{-6}	$m^2\,s^{-1}$
Water depth, h	40	m
Submersion depth, d_s	5	m
Tether length, Δl	32	m
PTO damping, b_{PTO}	0.628	$MN\,s\,m^{-1}$
PTO stiffness, k_{PTO}	3.91	$MN\,m^{-1}$
Mesh convergence period, T_v	16	s
Mesh convergence wave height, η_v	5	m
Mesh convergence wave theory	Stokes V	—
Force convergence period, T_v	16	s
Force convergence wave height, η_v	3	m
Force convergence wave theory	Stokes II	—

3.1. Wave height convergence

Convergence of the fluid mesh within the NWT is vital to ensure appropriate representation of wave propagation. This process can be divided into two parts: convergence in the x-direction, and convergence in the z-direction. The y-direction is assumed to be not as important due to the wave direction being in the x-direction.

In these simulations, the parameters in Table 3 were employed. The parameter, $\Delta x/\lambda$ is the number of cells per wavelength and is the parameter held constant in future simulations to ensure appropriate resolution. An initial guess of 4 cells per wave height in the z direction and 80 cells in the y direction were used. The measured wave height relative to the desired wave height as x resolution increases is given in Figure 3a. This set of simulations shows that after approximately 140 cells per wavelength, the wave height converges. The wave height ratio converges to around 1, and the z resolution was also checked for convergence. The number of cells per wave height, $\Delta z/\eta$, and the corresponding wave height relative to the desired wave height is shown in Figure 3b.

Mesh convergence is achieved at around 10 cells per wave height. The measured wave height is within 3% of the desired wave height, which indicates adequate resolution in the y direction.

3.2. Excitation force convergence

To improve the validity of the CFD model, the pressure force around the stationary buoy was measured and compared to BEM solutions. The resolution of a certain volume around the buoy was doubled, and the surface of the buoy had cells that were doubled again. The variable parameter used in these simulations to check for convergence was the distance d_m around the buoy in which the cell resolution was doubled. This distance d_m was varied and the resulting force on the buoy over time is given in Figure 4.

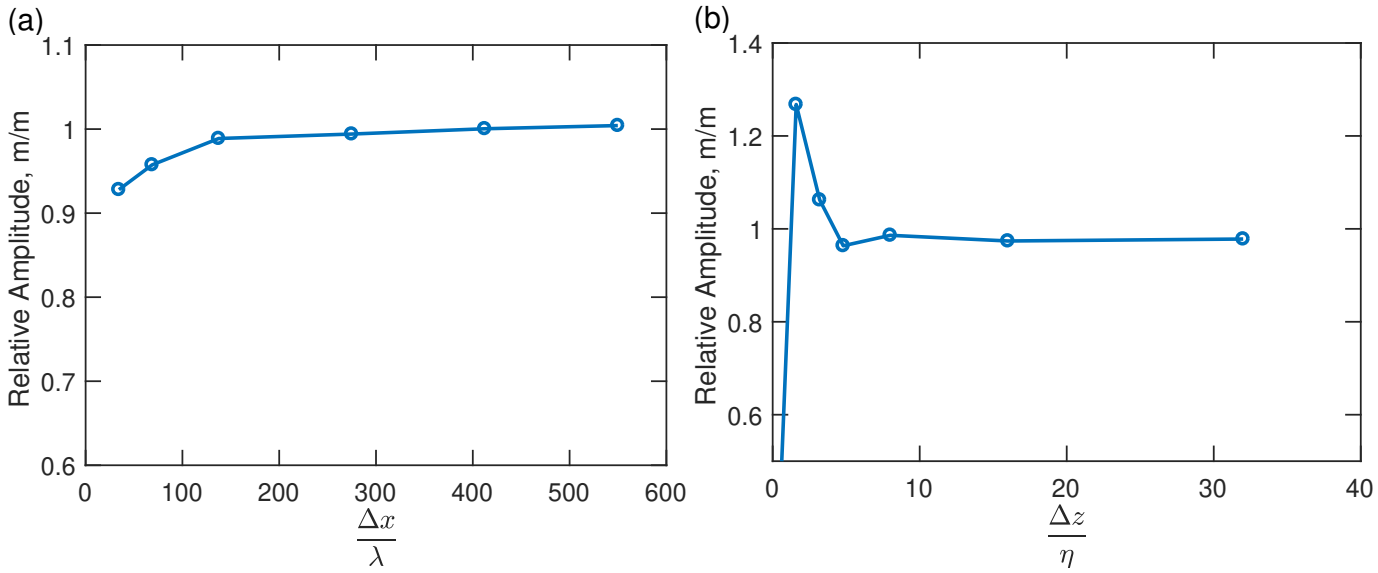

Figure 3: The wave height response when a given number of cells in the x (a) direction per wavelength and z (b) direction per wave height was used.

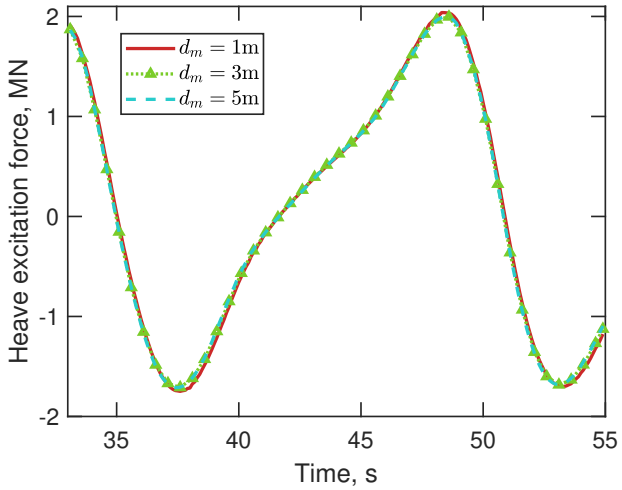

Figure 4: The time domain response of the force for various distances d_m around the mesh in which the mesh resolution was doubled.

The results show that the force converged when d_m reaches around 3m. However, results did not converge to the linear approximation (a sinusoid). Given the proximity of the buoy to the surface, it is expected to see a highly nonlinear result. It is therefore acceptable for the force convergence step that the linear and nonlinear forces do not match. The resulting mesh is shown in Figure 5.

3.3. Experimental comparison

To validate the CFD model, a comparison between simulation results and experimental data adopted from literature (Rafiee and Fiévez, 2015) was performed. The surge, heave, and pitch motion, along with the tether extension, tether velocity, and PTO force are provided in Figure 6. An arbitrary time offset (common for all plots) was applied for comparison purposes to ensure results are in phase.

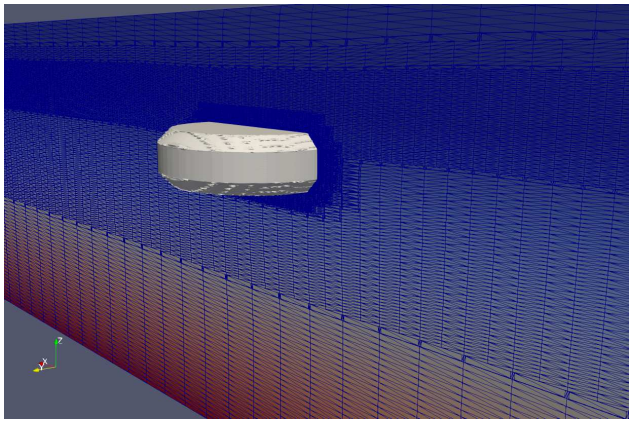

Figure 5: The NWT with the CETO-like buoy.

The results show that the CFD results and the experimental data follow much the same trend. Specifically, the tether extension, tether velocity, and PTO force give a strong match. The study providing the experimental data did not provide an estimation of experimental error, so an assumed 10% error is used based on common experimental setups (Windt et al., 2018). The Pearson correlation coefficients are a measure of linear dependence between two signals and may be used to quantify the difference between the experimental and numerical results. The correlation of these signals were calculated using the Matlab function *corrcoef*, and the signals were within 6% difference, excluding surge and pitch. The surge and pitch CFD results correlate to experimental values with 15% and -138% difference, respectively.

It is not uncommon for pitch CFD results to incorrectly replicate experimental results (Rafiee and Fiévez, 2015), possibly due to the assumption of uniform density in the CFD model. As surge and pitch motions are linked, this same error could also account for the slight discrepancy in the surge result as this is a secondary force and moment due to coupling of motion

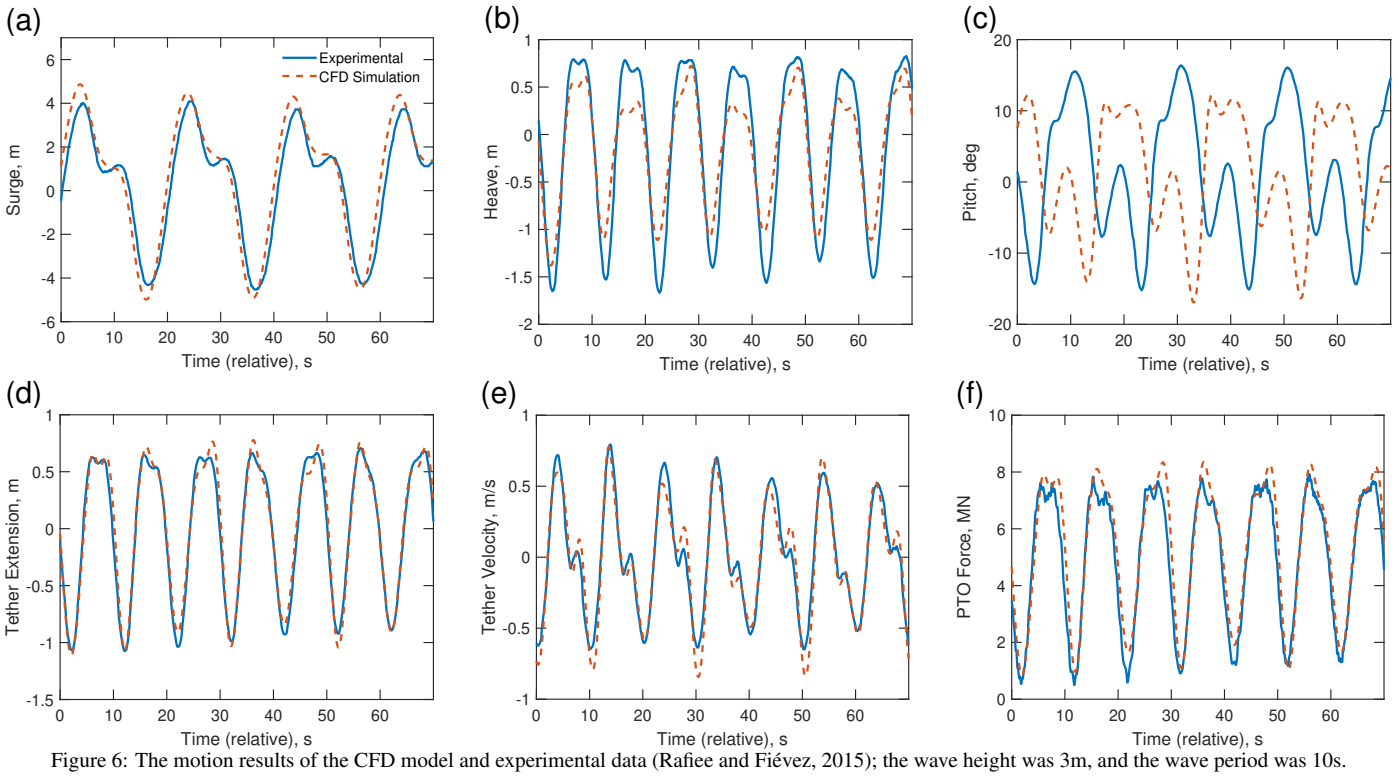

Figure 6: The motion results of the CFD model and experimental data (Rafiee and Fiévez, 2015); the wave height was 3m, and the wave period was 10s.

rather than a direct pressure effect. The established level of difference in heave motion and tether characteristics validates this CFD model, justifying the use of this model as a high fidelity comparison tool.

4. Simulation procedure

The validated CFD model provides a method to qualify and quantify the accuracy of the linear, partially nonlinear, and pseudo-nonlinear techniques. Three scenarios are proposed to determine the conditions influencing the fidelity of the pose dependent models.

The models constructed using linear, partially nonlinear, pseudo-nonlinear, and fully nonlinear methods were excited by regular waves over a range of frequencies. Due to computational resources, only a subset of frequencies were sampled for the CFD simulations. The parameters g, ρ, ν, h, and b_{PTO} were common in all simulations and scenarios. These parameters were used to calculate the linear hydrodynamic parameters in NEMOH. For each excitation frequency, a constant value of PTO damping was used, and the optimal PTO stiffness was calculated according to Equation (15).

The linear and pseudo-nonlinear methods assume constant drag coefficients. These drag coefficients are found in a previous study (Rafiee and Fiévez, 2015) which constructs and validates a CFD model. This study determines the drag coefficients by prescribing the motion of the body to oscillation in each DOF within the still numerical wave tank. The pressure force on experienced by the buoy, $\mathbf{F}_{\mathrm{p}}$ was quantified and curve fitting tools were then used to match the coefficients in the Morison equation given by

$$\mathbf{F}_{\mathrm{p}} = \mathbf{C}_I\ddot{\mathbf{x}} + \frac{1}{2}\rho\mathbf{C}_{\mathrm{D}}\mathbf{A}_{\mathrm{D}}\dot{\mathbf{x}}|\dot{\mathbf{x}}|\,, \tag{24}$$

where $\mathbf{C}_{\mathrm{I}}$ represents an inertial coefficient. The calculated drag coefficients are provided in Table 4.

Table 4: Drag coefficients.

	x	z	θ
Coefficient of drag, C_{D}	0.7	1.28	0.22

The scenarios are outlined in Table 5 and were constructed to determine the performance of the pseudo-nonlinear method for low amplitude oscillations and increased submergence depths. The range of values for the pseudo-nonlinear BEM hydrodynamics gain scheduling method was selected to suit the expected motion range.

Table 5: The scenario specific parameters.

Parameter	**Scenario 1**	**Scenario 2**	**Scenario 3**
Submergence depth, d_{s}	7 m	7 m	11 m
Wave height, η	1 m	0.2 m	1 m
Wave theory	Stokes II	Stokes I	Stokes II
BEM range, z (m)	-1 to 1	-0.1 to 0.1	-1 to 1
BEM range, θ (deg)	-15 to 15	-15 to 15	-15 to 15

The lookup table required for the pseudo-nonlinear method has a resolution of 13 sampled points linearly spaced between

the BEM range specified for heave and pitch. A total of 169 points were contained within the constructed lookup table. The variation due to surge ultimately manifests as the surge phase offset, σ_s, represented in Equation 6. The CFD simulations use the resolution found in Section 3. The periods and PTO stiffnesses for each scenario (denoted by subscripts 1, 2, and 3) used in the CFD simulations are provided in Table 6.

Table 6: Simulation conditions.

Period (s)	6	7	8	9	10	12	14
$k_{\text{PTO, opt 1}}$ (MN m^{-1})	3.33	3.32	3.48	3.18	2.51	1.62	1.12
$k_{\text{PTO, opt 2}}$ (MN m^{-1})	3.33	3.32	3.48	3.18	2.51	1.62	1.12
$k_{\text{PTO, opt 3}}$ (MN m^{-1})	4.38	3.48	2.89	2.39	1.94	1.32	0.95

5. Results

5.1. Hydrodynamic results from NEMOH

When the pose of the buoy changes, the corresponding hydrodynamics vary substantially. To characterise this change, the excitation forces for varying pitch positions and the added mass for varying heave positions are provided in Figures 7a and 7b, respectively.

The excitation force is known to have a much larger amplitude as the buoy approaches the surface. For a change in pitch angle, the change is less intuitive, leading to the formation of different peak force frequencies. As heave location increases, the magnitude of added mass increases. Similar trends are seen in the radiative damping. These features in the hydrodynamic parameters emphasise the limitation of standard linear modelling, that the nonlinearities in these hydrodynamic parameters are not included.

5.2. Linear conditions convergence

To initially check that all models converge to similar motions in linear conditions, the models with scenario 1 conditions were subject to a long period, low amplitude wave, with a stiffness such that operation was off-resonance. The parameters for this check for convergence for linear conditions are contained in Table 7 and the time domain results of the tether extensions are shown in Figure 8.

The CFD results for this convergence test show some evidence of transient effects. However, all the results converge to similar motion amplitudes, particularly the linear, partially nonlinear, and pseudo-nonlinear models. This provides some confidence in each model in producing consistent results for linear conditions.

Table 7: Parameters for model convergence under linear conditions.

Parameter	**Value**	**Units**
Water depth, h	40	m
Submersion depth, d_s	7	m
Tether length, Δl	30	m
Wave height, η	0.4	m
Wave Period, T_w	29	m
PTO damping, b_{PTO}	0.628	MN s m^{-1}
PTO stiffness, k_{PTO}	1.12	MN m^{-1}

5.3. Model dynamics

To benchmark the linear based systems, the first scenario consist of a shallow submersion depth and a relatively large amplitude wave (Table 5). Monochromatic waves were used to excite the WEC. The resulting motion for each monochromatic wave was analysed by finding the root mean square (RMS) of the oscillation. The RMS was used to incorporate the impact of multiple modes of oscillation present. Other important parameters to explore the performance of a WEC include the maximum PTO force, and the RMS of the instantaneous power generated. Transient effects for each simulation were discarded where practically possible to ensure the steady state operation of WEC was considered. Scenario 2 required the longest calculation time, some taking upwards of 47 days to complete. The simulation time of each scenario was selected to be 200s for each scenario, the most intensive mesh had 5319938 cells, and the simulation was parallelised over 32 CPU cores on a single node with Skylake Intel CPU architecture with 9665 MB of memory per CPU. For simulations with a wave period 14, only 14.2 periods were simulated and may have slight transient influences. Simulations with other wave periods were observed to have settled into a steady state. The motion RMS, maximum PTO force, and the power RMS for each scenario are shown in Figures 9a, 9b, 9c, 10a, 10b, 10c, 11a, 11b, and 11c, respectively.

Given the significant discrepancy between the linear based models and the CFD model, the combined hydrodynamic forces (excitation and radiation) from the linear models were compared with the pressure forces experienced by the buoy in the CFD model. The respective forces for Scenario 1, with a period of 10s were found and presented in Figure 12a. Furthermore, the forces for the same scenario when the linear models were subject to the CFD motion are given in Figure 12b. To further visualise the motion, images of the NWT during the motion are provided in Figure 13.

The linear simulations were conducted on a standard desktop computer, whereas the CFD simulations were conducted on the super computer Phoenix, hosted by The University of Adelaide. Each simulation was parallelised over 32 processors. Each scenario and period for the CFD simulations demonstrated different computational requirements, whereas the linear, partially nonlinear, and pseudo-nonlinear showed similar computation time. Scenario 1 with a period of 10s was selected as rep-

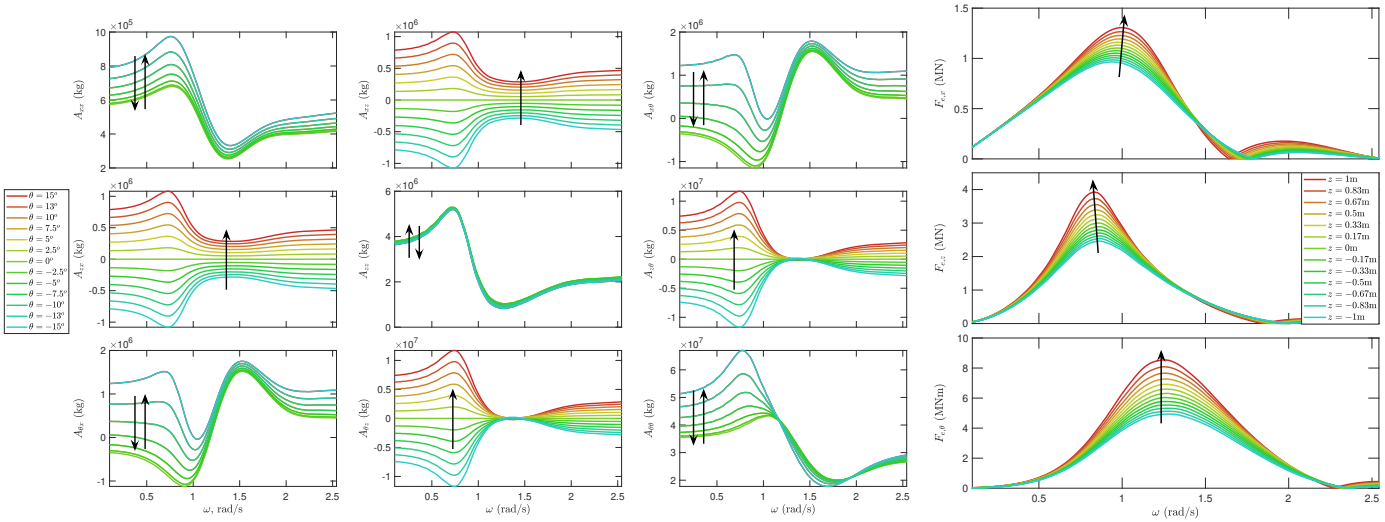

(a) Hydrodynamic added mass varying pitch orientations for $z = 0$.

(b) Excitation force varying heave for $\theta = 0$.

Figure 7: Example hydrodynamic added mass and excitation force for varying DOFs. The arrows indicate the direction of change of hydrodynamic added mass and excitation force as the respective DOFs are varied.

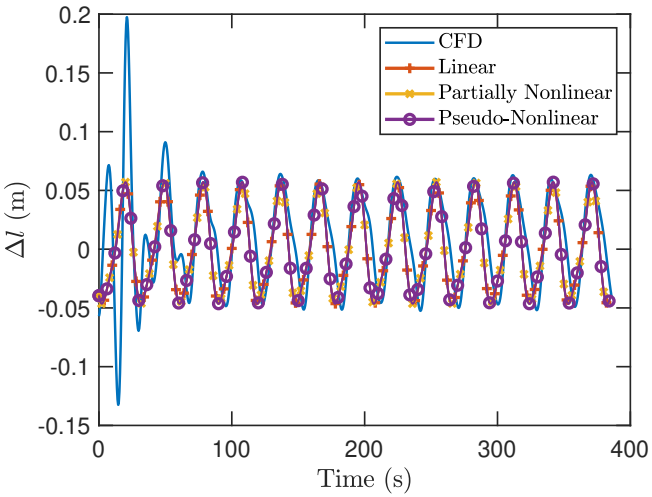

Figure 8: The time domain response of the tether extension when the buoy is excited a long period and low amplitude wave.

resentative of typical computation requirements and a comparison of the typical computational time for each model is given below in Table 8.

6. Discussion

In all three scenarios, the linear and partially nonlinear kinematics were almost identical. The most significant difference was seen in Scenario 1, specifically in the maximum PTO force where the partially nonlinear results approach the trend seen in the pseudo-nonlinear results (see Figure 9b). The pseudo-nonlinear results generally indicate a slightly larger amplitude motion response compared to all other models. The CFD results were found to generally have a lower motion RMS, maximum force, and power RMS with the exception of one frequency (see Figure 9a). The significant differences between the linear based

Table 8: Comparison of computation time.

Model	**Computation time (s)**
Linear	2.3
Partially nonlinear	3.8
Pseudo-nonlinear	30.0
CFD	388221 (4.5 days)

methods and the CFD indicate that for submerged WEC, the pose-dependent representations of the excitation and radiation forces are insufficient to describe the fluid-structure interaction even for linear wave conditions.

In Scenario 1, the peak in the surge motion is widened in the pseudo-nonlinear model, whereas the linear and partially nonlinear are almost indistinguishable. This indicates that the most influential change in the modelling methods was the pose-dependent radiation force representation. Additionally, the heave motion RMS of the pseudo-nonlinear method in some cases shifts towards the CFD results, while in others, shifts away, with no strong trend seen overall.

The most favourable condition in the CFD results is seen at the 9 s wave period, where the power RMS is largest in all models (see Figures 9c, 10c, and 11c). This may be due to strong interaction between heave and surge modes as both seem to be experiencing increased oscillations, as seen in Figure 9a. A peak in this frequency region is not predicted in the linear models, and therefore may arise from some inherently nonlinear phenomenon. The motion from the CFD model at this wave period is shown in Figure 13. These series of images depict how the body of water above the buoy oscillates up and down resulting in fluid rushing from all sides into the center creating a jet of water. In the situation shown, this occurrence is roughly in phase with the wave. Due to the phase relationship, this ef-

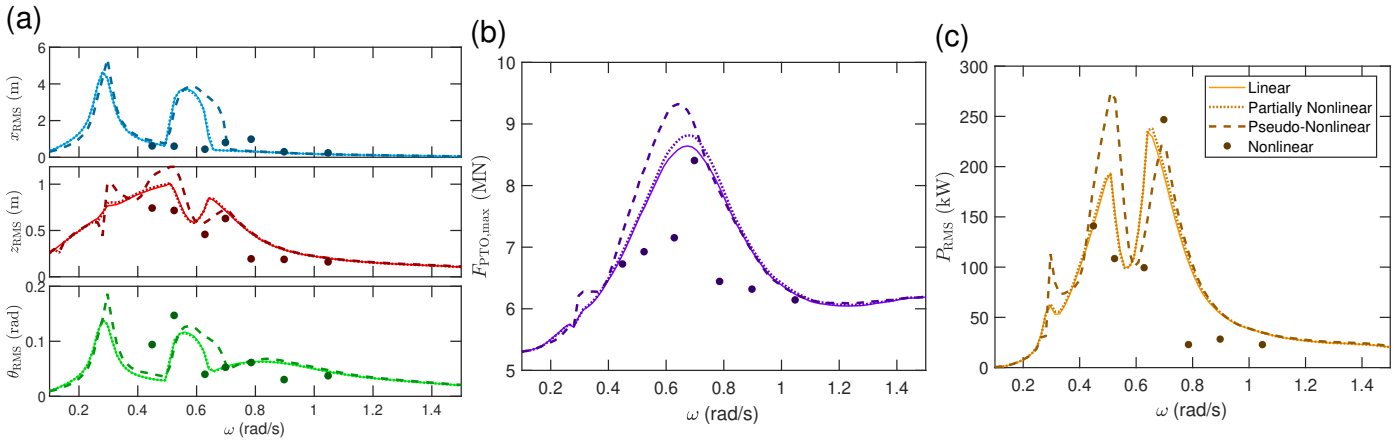

Figure 9: The performance characteristics of the WEC at varying excitation frequencies under Scenario 1 conditions for the linear (–), partially nonlinear (· · ·), pseudo-nonlinear (- - -), and fully nonlinear (CFD) (•) methods: (a) the RMS of the CETO-like buoy motions, (b) the maximum PTO force of the CETO-like buoy, (c) the power RMS of the CETO-like buoy.

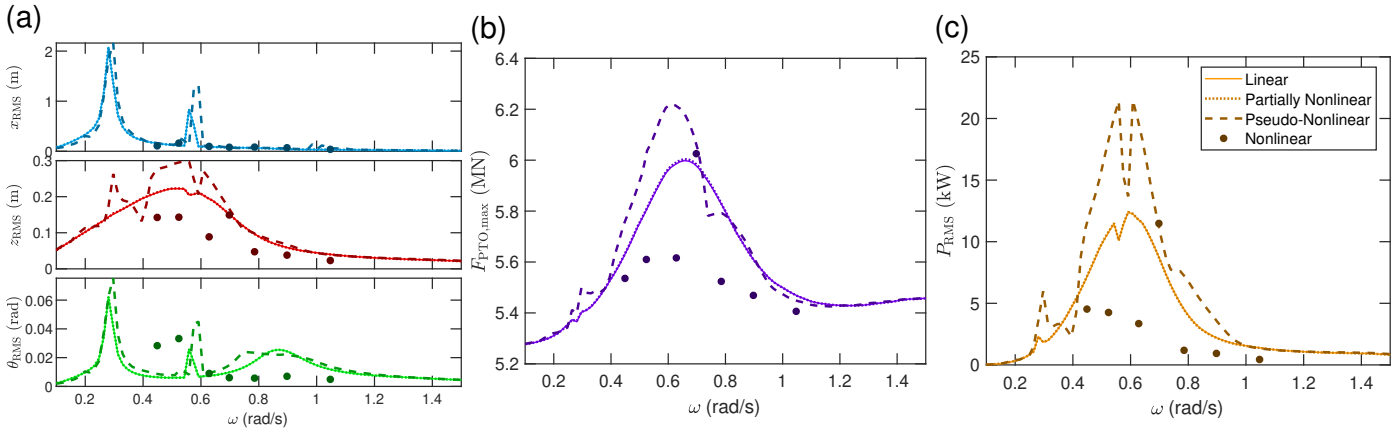

Figure 10: The performance characteristics of the WEC at varying excitation frequencies under Scenario 2 conditions for the linear (–), partially nonlinear (· · ·), pseudo-nonlinear (- - -), and fully nonlinear (CFD) (•) methods: (a) the RMS of the CETO-like buoy motions, (b) the maximum PTO force of the CETO-like buoy, (c) the power RMS of the CETO-like buoy.

fect may be acting to improve oscillation amplitude, whereas for other frequencies, this occurrence would not be in phase with excitation and therefore would destructively interfere with oscillations. This peak in performance is also seen in scenarios 2 and 3, indicating this effect is frequency dependent rather than amplitude or submergence depth dependent.

Similar shifts in motion RMS are seen in Scenario 2, where the heave motions are also changed, and the surge peaks have shifted slightly to higher frequencies. Under this lower amplitude excitation, the heave motion RMS in the pseudo-nonlinear method forms multiple peaks and shows a stronger coupling to surge and pitch motions. The trends of the PTO force in Scenario 2 are similar to the results from Scenario 1 in that the pseudo-nonlinear method predicts larger forces for low frequency waves and converges to the forces found in CFD simulations at higher frequency waves. The pseudo-nonlinear method shows more prominent peaks for the power generation performance but are generally poorer estimates of the CFD results than the other linear models.

When the submergence depth was increased in Scenario 3, the differences between the linear, partially nonlinear, and pseudo-nonlinear reduce. This aligns with the understanding that more hydrodynamic nonlinearity occurs closer to the surface. However, the trends of the linear results still do not typically follow the fully nonlinear results, indicating that the linear models do not account for important fluid interactions. The hydrodynamic pressure forces from CFD Scenario 1 with wave period of 9 s were compared with the combined excitation and radiation force simulated in the three linear models in Figure 12a to further understand what modelling deficiencies are present. These results show reasonably good matching between the heave hydrodynamic forces but a poor phase and amplitude match in the surge and pitch hydrodynamic forces. For these hydrodynamic forces, different trajectories were followed due to the different modelling methods. To eliminate this modelling discrepency, the linear models were subject to the motion seen in the CFD simulations and the resulting forces are given in Figure 12b. A large difference between all forces is seen, with the most inconsistent being the pseudo-nonlinear hydrodynamic force. The significant difference in pitch is thought to be due to transient effects and the result of the oscillating water above the buoy. Drag forces from the CFD simulations were found to be

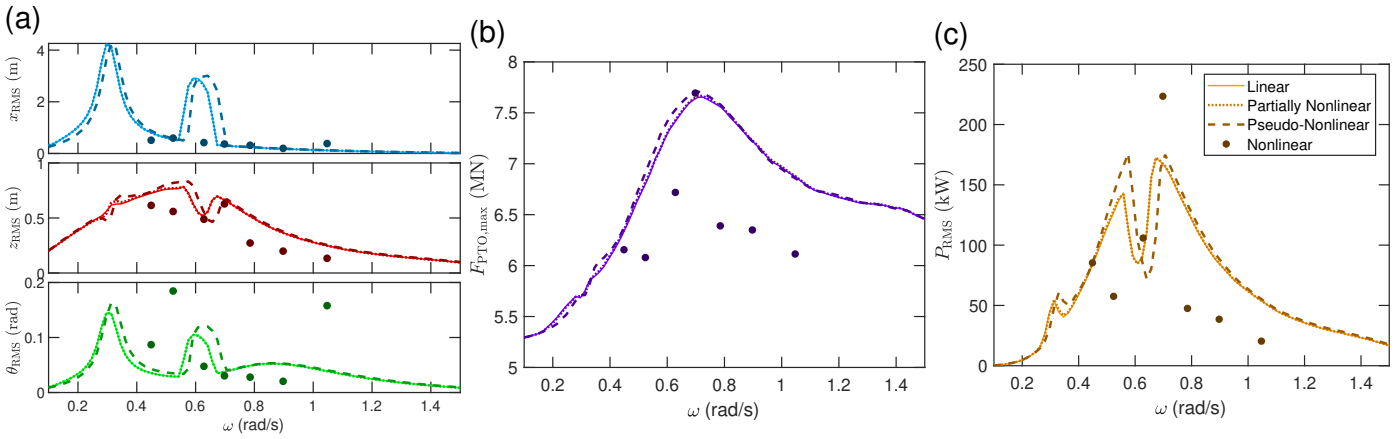

Figure 11: The performance characteristics of the WEC at varying excitation frequencies under Scenario 3 conditions for the linear (–), partially nonlinear (· · ·), pseudo-nonlinear (- - -), and fully nonlinear (CFD) (•) methods: (a) the RMS of the CETO-like buoy motions, (b) the maximum PTO force of the CETO-like buoy, (c) the power RMS of the CETO-like buoy.

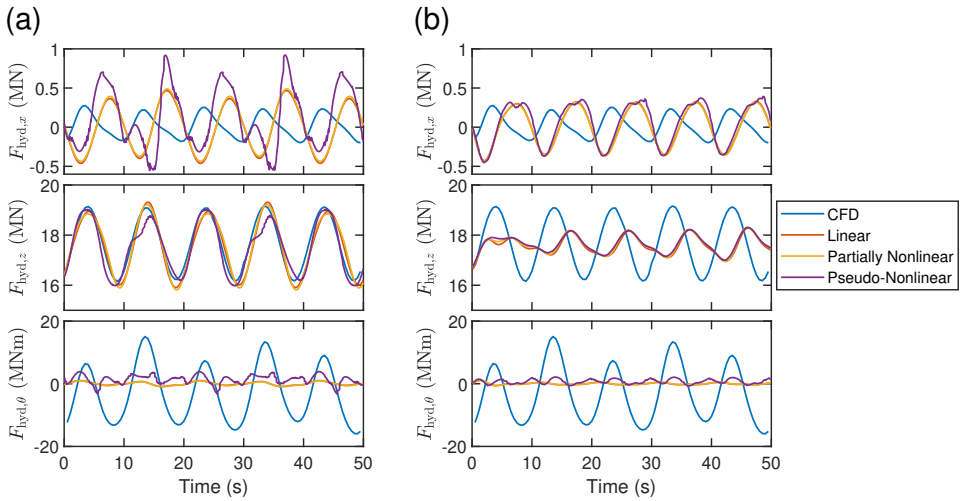

Figure 12: The combined hydrodynamic pressure forces of the linear, partially nonlinear, pseudo-nonlinear, and fully nonlinear models when subject to Scenario 1 conditions with a period of 10s: (a) resultant hydrodynamic forces during simulation of each model when the buoy trajectory is not constrained, and (b) resultant hydrodynamic forces during simulation of each model when the buoy trajectory is constrained to follow positions from CFD model.

negligible compared to the other hydrodynamic forces in this case. These results again show that linear methods are not capable of quantifying significant nonlinearities for a WEC of this shape and type.

The disparity between validated nonlinear CFD model and the pseudo-nonlinear and linear models demonstrate that the nonlinearity of the hydrodynamic excitation and radiation force is not the major nonlinearity in the system. The CFD model depicted in Figure 13 demonstrates that the fluid around the buoy is subject to some nonlinear flow characteristic as the body of fluid above the buoy seems to oscillate with the buoy rather than with the wave. The large diameter of the CETO buoy relative to the submergence depth may be the reason for this significant impact the fluid structure interaction leading to perturbation of the body of water above the oscillating buoy. This situation is not accounted for within the presented linear models and may be the source of the large discrepancy. For such systems, these linear models evidently lack the fidelity to appropriately replicate experimental results.

In practice, the full 6DOF system should be considered. For the purposes of this study, the axisymmetric submerged PA was restricted to 3DOF to further explore the use of linear potential flow models in representing the relevant hydrodynamics. It should be noted that this restriction prevents the model from predicting parametric excitation of roll, sway, and yaw modes of oscillation. These features could be implemented by extending the model to 3DOF, which is conceptually no more challenging but requires more computation.

The findings show that the excitation forces are not always the major nonlinearity for PA WEC, which disagrees with current understandings of PA considerations (Penalba et al., 2017a). Specifically, the pseudo-nonlinear method which includes the nonlinearity due to pose in the excitation and radiation forces is seen in this work to be inadequate for replicating the nonlinear results. For large flat submerged buoys, there seems to be a dominant nonlinearity in the coupling between the buoy and the body of water above the buoy. One recommendation arising from this work is to use the hydrodynamic forces from the CFD model and linear models to quantify the impact of the nonlinearity and construct an additional term to implement within

the linear model. Some possible approaches include regression techniques to parameterise parts of the nonlinear hydrodynamic interaction. This approach may approximate some nonlinear aspects seen in fully nonlinear systems and improve the fidelity and simulation speed of the overall model. Such models are important for design and optimisation purposes.

7. Conclusion

This study compared four models of a submerged PA WEC; specifically, linear, partially nonlinear, pseudo-nonlinear, and fully nonlinear models were presented. The linear uses hydrodynamic parameters calculated using linear BEM tools about a single nominal position, the partially nonlinear model uses the same linear tools to implement gain scheduling to introduce pose dependence in the excitation forces. The pseudo-nonlinear uses hydrodynamic parameters calculated for a range of orientations and positions to incorporate the nonlinear pose-dependence for excitation and radiation forces. The constructed fully nonlinear CFD model was validated against experimental data from literature. The comparison between models showed that in all cases, the linear based models were insufficient to quantify the nonlinear fluid-structure interactions. Specifically, a frequency dependent nonlinearity was identified as the body of water above the buoy oscillating. This oscillation caused significant disruption and the breakdown of linear wave approximations. The nonlinearity in the excitation force was small compared to the nonlinearity in the radiation force, but both excitation and radiation nonlinearities diminished with increased submergence depth. Introducing pose dependent hydrodynamic forces as presented in this paper tends to overestimate the motion. However, at higher frequencies the linear and nonlinear models converged to give similar results. Overall the identified difference in hydrodynamic forces is significant but seemed frequency dependent and periodic. If this nonlinearity can be quantified, it may be possible to implement into the linear models to improve the fidelity and speed leading to more suitable models for optimisation.

Acknowledgement

This work was supported with supercomputing resources provided by the Phoenix HPC service at the University of Adelaide. This research was supported by an Australian Government Research Training Program (RTP) Scholarship.

References

Chao Jiang, S., Gou, Y., Teng, B., and Zhi Ning, D. (2014). Analytical solution of a wave diffraction problem on a submerged cylinder. *Journal of Engineering Mechanics*, 140(1):225–232.

Chozas, J. (2015). International levelised cost of energy for ocean energy technologies an analysis of the development pathway and levelised cost of energy trajectories of wave, tidal and OTEC technologies. Technical report, Ocean Energy Systems.

Crooks, D. J. (2017). *Nonlinear hydrodynamic modelling of an oscillating wave surge converter*. PhD thesis, Queen's University Belfast.

Cruz, J. (2008). *Ocean Wave Energy*. Springer-Verlag Berlin Heidelberg, 1 edition.

Cummins, W. (1962). The impulse response function and ship motions. Technical report, David Taylor Model Basin, Washington DC.

Davidson, J., Giorgi, S., and Ringwood, J. V. (2015). Linear parametric hydrodynamic models for ocean wave energy converters identified from numerical wave tank experiments. *Ocean Engineering*, 103:31 – 39.

Drew, B., Plummer, A. R., and Sahinkaya, M. N. (2009). A review of wave energy converter technology. *Proceedings of the Institution of Mechanical Engineers, Part A: Journal of Power and Energy*, 223(8):887–902.

Falnes, J. (2002). *Ocean waves and oscillating systems: Linear interactions including wave-energy extraction*. Cambridge University Press.

Giorgi, G. and Ringwood, J. V. (2017a). Comparing nonlinear hydrodynamic forces in heaving point absorbers and oscillating wave surge converters. *Journal of Ocean Engineering and Marine Energy*, 4(1):25–35.

Giorgi, G. and Ringwood, J. V. (2017b). Relevance of pressure field accuracy for nonlinear Froude–Krylov force calculations for wave energy devices. *Journal of Ocean Engineering and Marine Energy*, 4(1):57–71.

Giorgi, G. and Ringwood, J. V. (2019). A compact 6-DoF nonlinear wave energy device model for power assessment and control investigations. *IEEE Transactions on Sustainable Energy*, 10(1):119–126.

Guerber, E., Benoit, M., Grilli, S. T., and Buvat, C. (2012). A fully nonlinear implicit model for wave interactions with submerged structures in forced or free motion. *Engineering Analysis with Boundary Elements*, 36(7):1151–1163.

Hardy, P., Cazzolato, B., Ding, B., and Prime, Z. (2016). A maximum capture width tracking controller for ocean wave energy converters in irregular waves. *Ocean Engineering*, 121:516 – 529.

Le Méhauté, B. (2013). *An introduction to hydrodynamics and water waves*. Springer Science & Business Media.

Letournel, L., Chauvigné, C., Gelly, B., Babarit, A., Ducrozet, G., and Ferrant, P. (2018). Weakly nonlinear modeling of submerged wave energy converters. *Applied Ocean Research*, 75:201–222.

MathWorks (2019). Matlab control system toolbox: Lpv system. https://au.mathworks.com/help/control/ref/lpvsystem.html. The MathWorks, Natick, MA, USA.

McCabe, A., Aggidis, G. A., and Stallard, T. (2006). A time-varying parameter model of a body oscillating in pitch. *Applied Ocean Research*, 28(6):359–370.

Merigaud, A., Gilloteaux, J.-C., and Ringwood, J. V. (2012). A nonlinear extension for linear boundary element methods in wave energy device modelling. In *Volume 4: Offshore Geotechnics; Ronald W. Yeung Honoring Symposium on Offshore and Ship Hydrodynamics*. ASME.

Orszaghova, J., Wolgamot, H., Draper, S., Taylor, R. E., Taylor, P. H., and Rafiee, A. (2019). Transverse motion instability of a submerged moored buoy. *Proceedings of the Royal Society A: Mathematical, Physical and Engineering Sciences*, 475(2221):20180459.

Papillon, L., Wang, L., Tom, N., Weber, J., and Ringwood, J. (2019). Parametric modelling of a reconfigurable wave energy device. *Ocean Engineering*, 186:106105.

Penalba, M., Giorgi, G., and Ringwood, J. V. (2017a). Mathematical modelling of wave energy converters: A review of nonlinear approaches. *Renewable and Sustainable Energy Reviews*, 78:1188–1207.

Penalba, M., Kelly, T., and Ringwood, J. V. (2017b). Using NEMOH for modelling wave energy converters: A comparative study with WAMIT. *Centre for Ocean Energy Research (COER), Maynooth University, Co. Kildare, Ireland.*

Penalba, M., Mérigaud, A., Gilloteaux, J.-C., and Ringwood, J. V. (2017c). Influence of nonlinear froude–krylov forces on the performance of two wave energy points absorbers. *Journal of Ocean Engineering and Marine Energy*, 3(3):209–220.

Penalba, M. and Ringwood, J. V. (2019). Linearisation-based nonlinearity measures for wave-to-wire models in wave energy. *Ocean Engineering*, 171:496–504.

Perez, T. and Fossen, T. I. (2009). A Matlab toolbox for parametric identification of radiation-force models of ships and offshore structures. *Modeling, Identification and Control: A Norwegian Research Bulletin*, 30(1):1–15.

Rafiee, A. and Fiévez, J. (2015). Numerical prediction of extreme loads on the CETO wave energy converter. In *Proceedings of the 11th European Wave and Tidal Energy Conference, Nantes, France*.

Schubert, B. W., Meng, F., Sergiienko, N. Y., Robertson, W., Cazzolato, B. S., Ghayesh, M. H., Rafiee, A., Ding, B., and Arjomandi, M. (2018). Pseudo-nonlinear hydrodynamic coefficients for modelling point absorber wave en-

ergy converters. In *The 4th Asian Wave and Tidal Energy Conference, Taipei*.

Sergiienko, N., Rafiee, A., Cazzolato, B., Ding, B., and Arjomandi, M. (2018). Feasibility study of the three-tether axisymmetric wave energy converter. *Ocean Engineering*, 150:221–233.

Windt, C., Davidson, J., and Ringwood, J. V. (2018). High-fidelity numerical modelling of ocean wave energy systems: A review of computational fluid dynamics-based numerical wave tanks. *Renewable and Sustainable Energy Reviews*, 93:610–630.

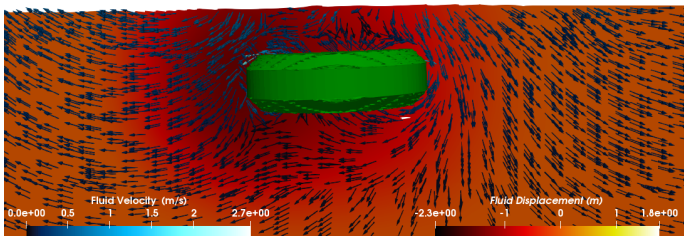

(a) $t = 50$ s.

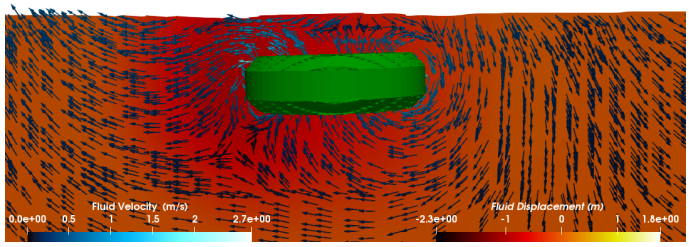

(b) $t = 51$ s.

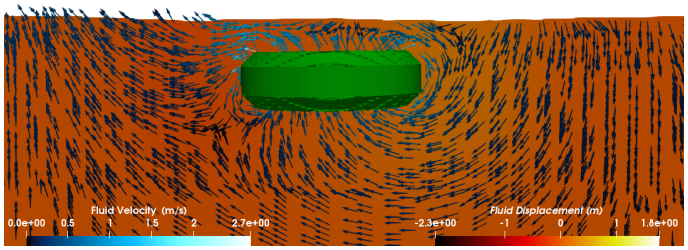

(c) $t = 52$ s.

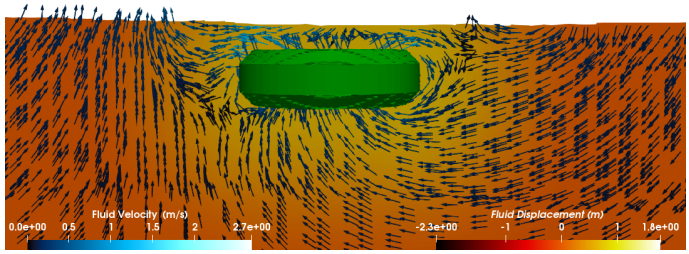

(d) $t = 53$ s.

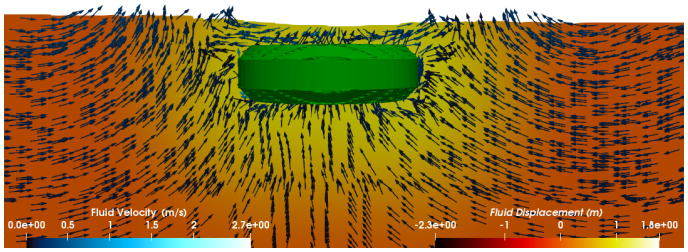

(e) $t = 54$ s.

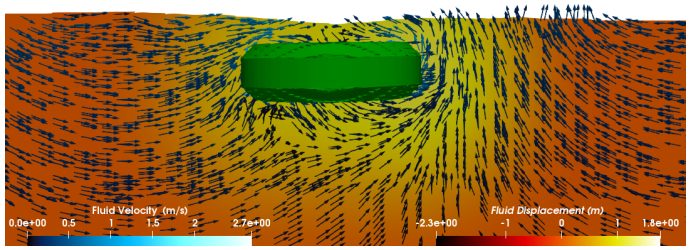

(f) $t = 55$ s.

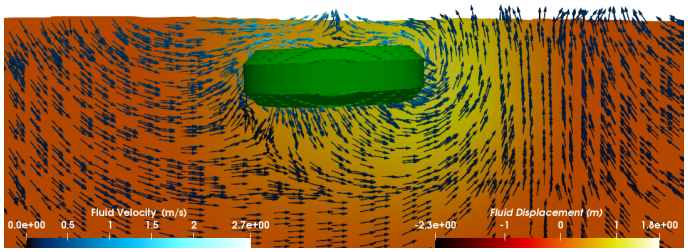

(g) $t = 56$ s.

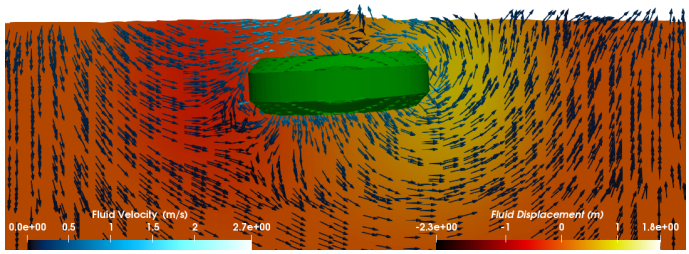

(h) $t = 57$ s.

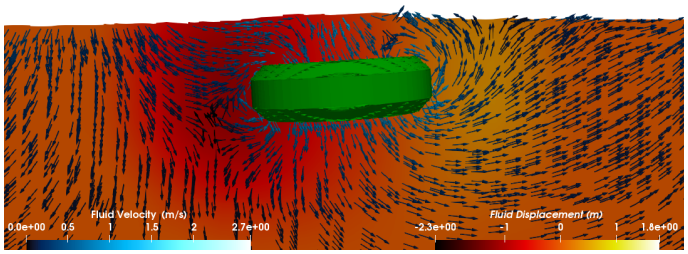

(i) $t = 58$ s.

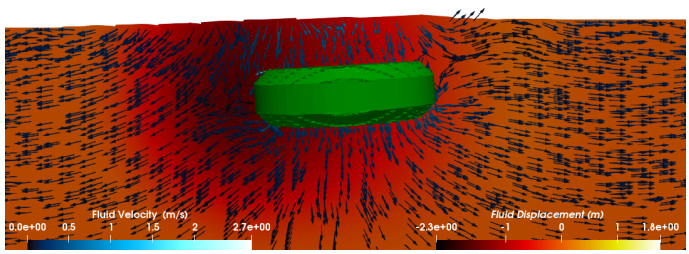

(j) $t = 59$ s.

Figure 13: The buoy in the NWT during operation. The fluid velocity and position are shown for Scenario 1 conditions with a 9 s period wave.